Eng. Sci., 2022, **17**, 242–255

Engineered Science

DOI: https://dx.doi.org/10.30919/es8d532

Realization of Electrochemically Grown α-Fe_2O_3 Thin Films for Photoelectrochemical Water Splitting Application

Avinash V. Rokade,[1,6*] Yogesh A. Jadhav,[1] Sagar Jathar,[1] Swati Rahane,[1] Sunil Barma,[1] Ganesh K. Rahane,[1] Sachin Thawarkar,[1] Priti Vairale,[1] Ashvini Punde,[1] Shruti Shah,[1] Sachin R. Rondiya,[2] Nelson Y. Dzade,[2] Bidhan Pandit,[3] Jayant Pawar,[4] Anurag Roy[5] and Sandesh Jadkar[6,*]

Abstract

Hematite ferric oxide (α-Fe_2O_3) based photoanode has emerged as a potential candidate for water splitting application due to its high absorption coefficient in the visible region and favorable band alignment. In the present work, α-Fe_2O_3 thin film photoanodes were fabricated using a cost-effective and straightforward electrodeposition technique. The crystal structure, phase purity, elemental composition, and formation of α-Fe_2O_3 were confirmed by X-ray diffraction (XRD), photoluminescence (PL), X-ray photoelectron spectroscopy (XPS), Raman spectroscopy, energy-dispersive X-ray spectroscopy (EDS), and scanning electron microscopy (SEM). The band gap calculated from the absorption spectrum from UV-visible analysis of α-Fe_2O_3 exhibited a significant absorption in the visible region. The α-Fe_2O_3 photoanodes were further characterized for their photoelectrochemical (PEC) properties along with electrochemical impedance spectroscopy (EIS) analysis. Furthermore, XRD, SEM, and Fourier transform infrared (FTIR) spectroscopy investigations were performed after photoelectrochemical measurement to ensure the stability of photoanodes. Also, the prepared photoanode was highly stable against a large range of pH conditions, and no photobleaching was observed for up to 30 min. Furthermore, a significant enhancement in the photocurrent conversion efficiency with an optimum film thickness was observed upon light illumination. A maximum photon conversion efficiency of 1.44 % was obtained with a photocurrent density of 6.25 mA/cm^2 for 1 V vs. saturated calomel electrode (SCE) under the simulated solar light.

Keywords: α-Fe_2O_3; Electrodeposition; Water Splitting; Photoelectrochemical; Photoanode; Stability; Solar Energy.
Received: 18 June 2021; Revised: 15 September 2021; Accepted: 15 September 2021.
Article type: Research article.

1. Introduction

Gradually increasing demand for fossil fuels, residual carbon footprint, and adverse environmental impact have exerted enormous pressure on the already stretched world energy infrastructure. It is challenging to meet the ever-rising energy demand of growing economies due to the limited nature of fossil fuels. The emission of polluting gases such as CO_2, CO, nitrogen oxides, sulfur dioxide, and other volatile organic compounds is significant. The improved standards of living and rapid industrialization have expedited the research in clean, eco-friendly, and low-cost energy harvesting technologies. Among all possible alternative energy sources, solar water-splitting (H_2 and O_2 evolution) offers a great promise to fulfill the growing energy needs sustainably.[1] However, water splitting using semiconductor photoanodes requires a suitable bandgap, high chemical stability, and low kinetic overpotential. Moreover, appropriate band edge positions for H_2 and O_2 evolution and favorable charge transfer at the semiconductor/electrolyte interface play a crucial role in achieving high water splitting efficiencies.[2,3]

The phenomenon of solar hydrogen evolution *via* water splitting was first demonstrated using single-crystal titania (TiO_2) as a photoanode with a bandgap of 3.2 eV by Fujishima and Honda in 1972.[4] However, the large bandgap (3.2 eV) limits its light absorption only in the ultra-violet (UV) region. Moreover, ZnO has been demonstrated as a prominent photoanode material with a bandgap similar to TiO_2 but has a much higher absorption coefficient (10^4-10^5 cm^{-1}) and a very high electron carrier mobility (~ 155 cm^{2}s^{-1}V^{-1}).[5,6] However, the wide bandgap and inferior charge transport properties of

[1] *School of Energy Studies, Savitribai Phule Pune University, Pune 411007, India.*
[2] *School of Chemistry, Cardiff University, Main Building, Park Place, Cardiff, CF10 3AT, Wales, UK.*
[3] *Department of Materials Science and Engineering and Chemical Engineering, Universidad Carlos III de Madrid, Avenida de la Universidad 30, 28911 Leganés, Madrid, Spain.*

these materials restrict their use in high-performance photoelectrochemical (PEC) applications. However, the narrow bandgap semiconductor materials such as CdS,[7] PbS,[8] CdSe,[9] Fe_2O_3,[10] Cu_2SnS_3,[11] and Cu_2O[12] have been extensively explored for absorption in the visible region and to reduce the recombination of photo-generated charge carriers. Recently, ferric oxide (Fe_2O_3) has attracted significant consideration as a crucial photocatalytic material due to its narrow bandgap (~ 2.0 eV), high absorption coefficient (~ 10^4 cm^{-1}), and suitable band edges.[13,14] Furthermore, it is inexpensive, naturally abundant, non-toxic, thermo-chemically stable in the aqueous environment, and has good environmental acceptability.[15,16] It has been explored for a variety of applications such as Li-ion batteries,[17,18] supercapacitors,[19] peroxide sensors,[20] solar energy conversion via water splitting,[21] dye degradation,[22] water purification, and treatment.[23,24] Thin films of Fe_2O_3 have been prepared by various methods such as chemical vapor deposition,[25] sol-gel processes,[26] pulsed laser evaporation,[27] reactive sputtering,[28] hydrothermal method,[29] spray pyrolysis,[30,31] *etc*.

The pristine Fe_2O_3 photoanodes have been studied for photocatalytic water splitting. However, a short excited-state lifetime[32–34] and a small hole diffusion length (2-20 nm)[35,36] restrict its commercial adaptations. The drawbacks can be overcome by using a suitable synthesis method to obtain Fe_2O_3 thin films with excellent stability and thickness control to achieve minimum charge transfer resistance and reduce the recombination with rapid charge carrier collection. The maximum theoretical solar-to-hydrogen (STH) conversion efficiency at standard solar illumination for Fe_2O_3 has been reported at ~ 15 %.[13,37] Even though significant progress in Fe_2O_3 has been achieved, the performance improvement of various preparation strategies is still limited to committing 1-2 % efficiency so far. In this report, an attempt has been made to prepare stable and compact Fe_2O_3 thin films by using a facile and inexpensive electrochemical deposition method that can withstand low applied potential and a wide range of pH conditions. Apart from preparing stable films, the potential cycle was varied as 10, 20, 30, and 40 cycles to achieve an optimum thickness. As a result, efficient Fe_2O_3 photoanode films that can absorb most of the solar spectrum and benefit PEC water splitting can be obtained. As a result, we observed that the optical properties of Fe_2O_3 films, namely band gap, band edge positions, and absorption of the prepared film, could be tuned just by varying potential cycles. Thus, the maximum photon conversion efficiency of 1.44% corresponding to a photocurrent density of 6.25 mA/cm^2 at 1 V_{SCE} for a film with 20 potential cycles has been observed. As per our knowledge, it is one of the best-reported photoresponses for α-Fe_2O_3-based PEC devices using the same electrodeposition technique. In addition to this, excellent stability of the prepared photoanode (scotch tape test) is achieved, which is further reconfirmed by XRD, FTIR, and SEM-EDS analysis after the electrochemical activity.

[4] *Krishna Institute of Medical Sciences, Deemed to be University, Karad 415110, India.*

[5] *Environment and Sustainability Institute, University of Exeter, Penryn Campus Cornwall TR10 9FE, UK.*

[6] *Department of Physics, Savitribai Phule Pune University, Pune 411007, India.*

**Email:* avinashrokade12@gmail.com (A. Rokade), sandesh@physics.unipune.ac.in (S. Jadkar)

2. Experimental details

2.1 Chemicals

Ferric chloride ($FeCl_3$), potassium fluoride (KF), potassium chloride (KCl), and hydrogen peroxide (H_2O_2) were used as received without any further purification.

2.2 Preparation of Fe_2O_3 photoanode

The method employed for the thin film preparation of α-Fe_2O_3 is the electrochemical deposition technique, which offers the facile synthesis route with control over film thickness *vs*. deposition cycle, low cost, uniform large-area deposition, and room temperature deposition. Moreover, the electrochemical deposition technique is a robust one, with no skilled labor required. The chemicals required for deposition are only cheap metal salts and water. Compared to other deposition techniques such as spin coating, doctor blade, chemical bath deposition (CBD), successive ionic layer adsorption and reaction (SILAR), sol-gel, spray pyrolysis, hydrothermal, *etc*., the electrochemical deposition technique offers more advantages over others for the deposition of semiconductor junction thin films. Moreover, the electrodeposition technique helps conduct thin film deposition over a large area with good uniformity. For the synthesis of Fe_2O_3 thin films, fluorine-doped tin oxide (FTO) coated glass substrates (2 cm × 1 cm) with a sheet resistance ~of 15 Ωcm^{-1} and thickness ~of 150 nm were used. Firstly, the FTO-coated glass substrate was sequentially cleaned using acetone, ethanol, and distilled water in an ultrasonicator for 5 minutes each. Then, the chemical solution was prepared by using an aqueous electrolyte of 0.05 M $FeCl_3$, 0.05 M KF, 0.1 M KCl, and 1 M H_2O_2. The electrochemical deposition was performed using an Autolab potentiostat (Model-N302) controlled in a three-electrode cell configuration system. FTO glass substrate, saturated calomel electrode (SCE), and Pt were used as working, reference, and counter electrodes. The thickness of Fe_2O_3 thin films during electrodeposition is controlled by changing the number of deposition cycles.

The Fe_2O_3 thin films were deposited on the FTO substrate using the cyclic voltammetry with different potential cycles of 10, 20, 30, and 40 and were named Fe-10, Fe-20, Fe-30, and Fe-40, respectively. The potential during voltammetry was varied from -0.2 to 0 V (at a scan rate of 20 mV/s) at room temperature. The obtained films were annealed at 600 °C in an ambient atmosphere for 1 hr to obtain pure phase α-Fe_2O_3 thin films. Fig. 1(a) shows the schematic of the

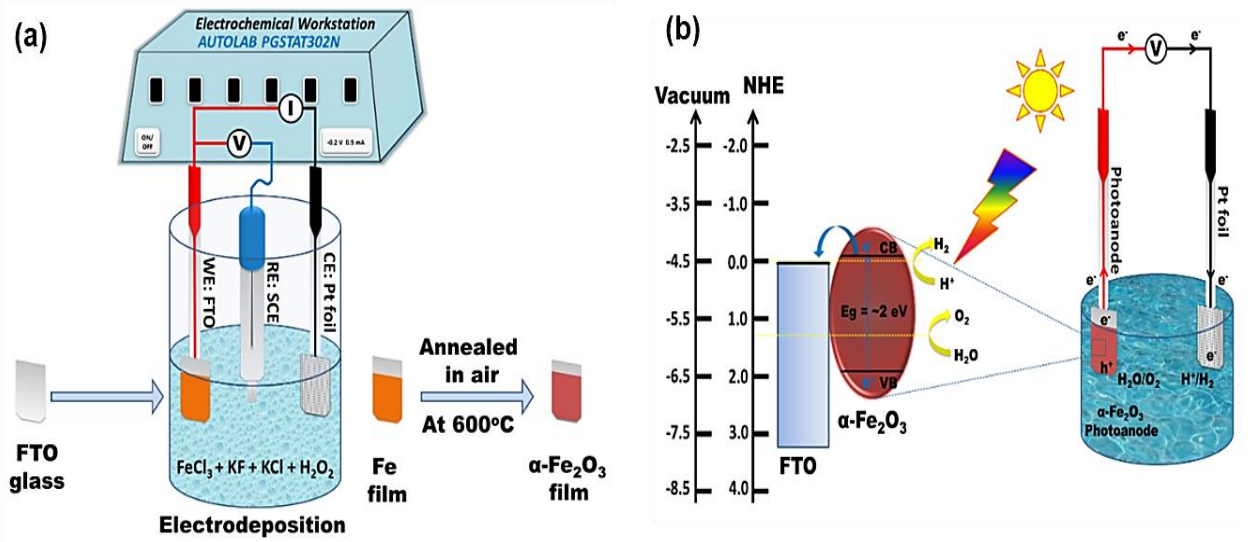

Fig. 1 Schematic representation (a) electrochemical deposition method employed to prepare α-Fe_2O_3 thin films; and (b) PEC water splitting mechanism.

electrochemical deposition method for the preparation of Fe_2O_3 thin films on the FTO substrate. The Fe_2O_3 thin films deposited on an FTO glass were used as photoanode for PEC water splitting measurements in an aqueous electrolyte.

2.3 Material characterizations

XRD analysis of the prepared photoanodes was carried out using Bruker D8 Advance, Germany diffractometer equipped with a Cu Kα irradiation source (λ = 0.154 nm). Scanning electron microscopy (SEM) was used to analyze the samples' surface morphology using a JEOL JSM 6360A SEM equipped with energy-dispersive x-ray spectroscopy (EDS) with an operating voltage of 20 kV. The electronic absorption spectra were recorded using a JASCO V-670 UV-Visible spectrophotometer ranging from 450 to 700 nm to determine the bandgap and absorption band edges. Raman spectra were recorded with a Raman spectrophotometer (Horibra-Jobin Yvon LABRAM-HR) with a 532.8 nm He-Ne laser excitation source. The Raman laser power was kept at less than 5 mW to avoid laser-induced crystallization on the films. The steady-state photoluminescence (PL) spectra were recorded using Edinburgh Instruments FLS 980 spectrophotometer. The samples were excited using a 580-600 nm line for recording steady-state PL. The FTIR spectra were recorded in a transmission mode using an FTIR spectrophotometer (JASCO, 6100-type A) in the range 550-4000 cm^{-1}. The x-ray photoelectron spectra (XPS) were recorded using a Kratos Axis Ultra DLD photoelectron spectrometer instrument with a total energy resolution ~ of 0.9 eV fitted with an Al K$_\alpha$ radiation source (soft X-ray source at 1486.6 eV) at base vacuum >10^{-9} Torr. The XPS signal was obtained after several scans in the acquisition process. The spectra were recorded for the specific elements (Fe, O).

2.4 Photoelectrochemical study

Figure 1(b) illustrates the PEC water-splitting mechanism. The PEC measurement was carried out in a standard three-electrode configuration with the Fe_2O_3 photoanode as the working electrode, Pt plate as counter-electrode, and saturated calomel electrode (SCE) as reference electrode using a computer-controlled potentiostat (AUTO LAB PGSTAT302N, Metrohm make) equipped with a frequency response analyzer (FRA). An aqueous solution of 1 M NaOH was used as an electrolyte with a pH of 13. A solar simulator with a 150 W Xenon light source (PEC-L01) with an illumination intensity of 100 mW/cm^2 was used to illuminate the surface of the photoanodes under light for current density-voltage (J-V), current density-time curves along with the electrochemical impedance spectroscopy (EIS) analysis. The impedance spectra were recorded under the light condition at 0.5 V *vs*. SCE applied potential with an alternating current (AC) modulation amplitude of 10 mV in the 0.1 Hz to 1 MHz frequency range. The J-V curves were measured with a 50 mV/s scan rate from -0.5 to 1.0 V *vs*. SCE.

3. Results and discussion

3.1 X-ray diffraction (XRD) analysis

XRD measurements were carried out to understand the crystal phase and structure of as-deposited Fe_2O_3 films. Fig. 2 shows the XRD pattern of the Fe_2O_3 thin films deposited with 10, 20, 30, and 40 potential cycles, which are denoted by Fe-10, Fe-20, Fe-30, and Fe-40, respectively. The presence of multiple peaks in the XRD pattern points to the polycrystalline nature of Fe_2O_3 films.

As seen from the XRD patterns, the prominent diffraction peaks were observed at 2θ ~ 24.2°, 33.2°, 35.5°, 40.9°, 49.46°, 54.5° and 63.99° corresponding to (012), (104), (110), (113), (024), (116) and (300) diffraction planes, respectively. These peaks show a good agreement with the hexagonal crystal structure of α-Fe_2O_3 (JCPDS data file # 33-0664). The asterisk symbols (*) represent the diffraction peaks obtained from the FTO substrate. It is clear from the XRD pattern that the

observed peaks correspond to the pure α-Fe_2O_3 phase without any secondary phases. Similar diffraction peaks were reported by *Wei et al.*[38] for Fe_2O_3 films prepared by rapid thermal oxidation and by *Wu et al.*[39] for Fe_2O_3 films prepared by microwave-assisted hydrothermal process. The lattice parameters (i.e., a = 5.03 Å and c = 13.7 Å) show excellent agreement with the standard values reported for the α-Fe_2O_3 crystal structure.

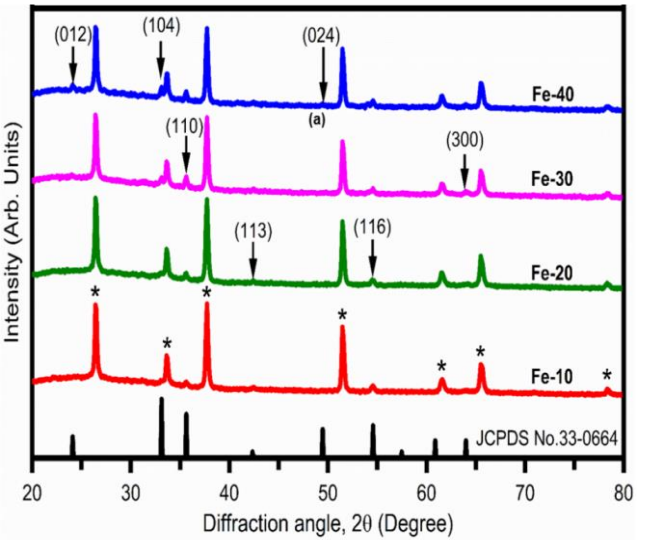

Fig. 2 XRD pattern of α-Fe_2O_3 films deposited on FTO at different potential cycles in the electrochemical deposition method.

The crystallite size (d) was calculated from the (110) peak using *Debye-Scherrer's* equation as shown in Equation (1):[40]

$$d = \frac{0.9\,\lambda}{\beta\cos\theta} \quad (1)$$

where λ is the x-ray source wavelength, β is the full width at half maximum (FWHM), and θ represents Bragg's diffraction angle. The estimated average crystallite size is equal to ~ 29 nm for the Fe-40 cycles sample. Although the α-Fe_2O_3 structure is observed for all the samples, a sample with fewer cycles (Fe-10) shows a relatively lower peak intensity due to low deposition. However, the phase formation and appearance of all the peaks are consistent for all the samples, which indicates that the potential cycles play an essential role in forming the crystalline phase of α-Fe_2O_3.

3.2 Raman spectroscopy analysis

Raman spectroscopy is a robust characterization method used to detect various material phases based on discrete vibrational modes. Different phases of Fe_2O_3 exhibit different characteristic phonon modes in Raman spectra, confirming the phase-type and purity of the material. The Raman vibrational spectra of Fe_2O_3 films deposited on FTO at different potential cycles in the electrochemical deposition method in the range 100-800 cm^{-1} are shown in Fig. 3. For all films, the Raman spectrum shows the major peaks at ~ 226, 245, 292, 409, 497, 611 and 660 cm^{-1}. Raman peaks located at ~ 226 and ~ 497 cm^{-1} correspond to the A_{1g} mode, whereas all other peaks located at ~ 245, ~ 292, ~ 409, ~ 611, and ~ 660 cm^{-1} correspond to the E_g mode of α-Fe_2O_3. These results are in good agreement with the characteristic Raman spectrum of pristine α-Fe_2O_3 crystals with a hexagonal structure that displays two A_{1g} and five E_g phonon modes.[41,42] These findings confirm the high purity of the synthesized α-Fe_2O_3 as no other peaks for Fe_2O_3 or oxyhydroxides are detected. The XRD results further validate this.

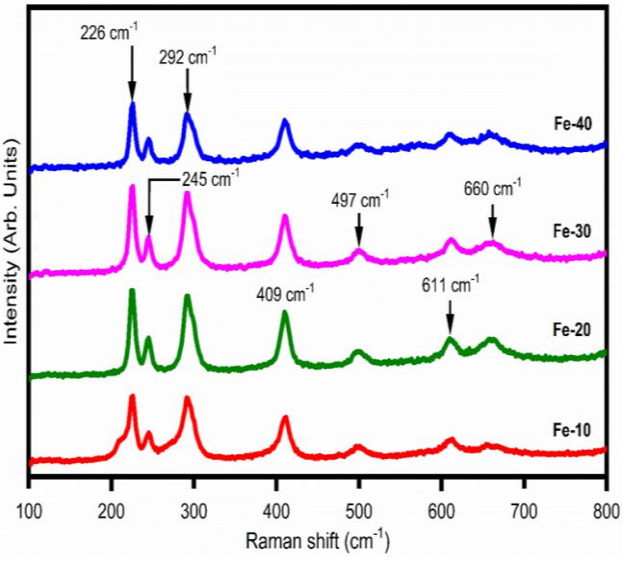

Fig. 3 Raman spectra of α-Fe_2O_3 films deposited at different potential cycles in the electrochemical deposition method.

3.3 Scanning electron microscopy analysis

The surface morphology of α-Fe_2O_3 films is studied using SEM analysis. Figs. 4(a1) - (a4) shows the SEM micrographs of α-Fe_2O_3 thin films deposited with 10, 20, 30, and 40 potential cycles. The α-Fe_2O_3 thin films deposited with 10 and 20 potential cycles (Figs. 4(a1) and (a2)) show granular morphology with uniform and dense growth of Fe_2O_3 on FTO substrate with minor defects such as cracks, pinholes, and protrusions. However, the films deposited with higher deposition cycles such as 30 and 40 (Figs. 4(a3) and (a4)) demonstrate several notches on the film surface.

The appearance of cuts on the film surface may be due to the interfacial stress between Fe_2O_3 and FTO substrate. The compositional analysis of α-Fe_2O_3 films was carried out using the EDS technique. Figs. 4(b1) - (b4) shows the typical EDS spectra of α-Fe_2O_3 films prepared with different potential cycles. These results indicate that Fe and O elemental composition is in the ratio ~of 2:3 for all the films, which agrees with the stoichiometric ratio. Figs. 4(c1 - c4) shows the cross-sectional SEM images of α-Fe_2O_3 films deposited by the electrochemical deposition method with various potential cycles. When the potential cycle during the electrodeposition process of samples Fe-10 to Fe-40 was increased from 10 to 40, the cross-sectional images of thin films indicate a linear change in thickness from 410 to 1040 nm, which agreed with the results reported by *Zhou et al.*[43]

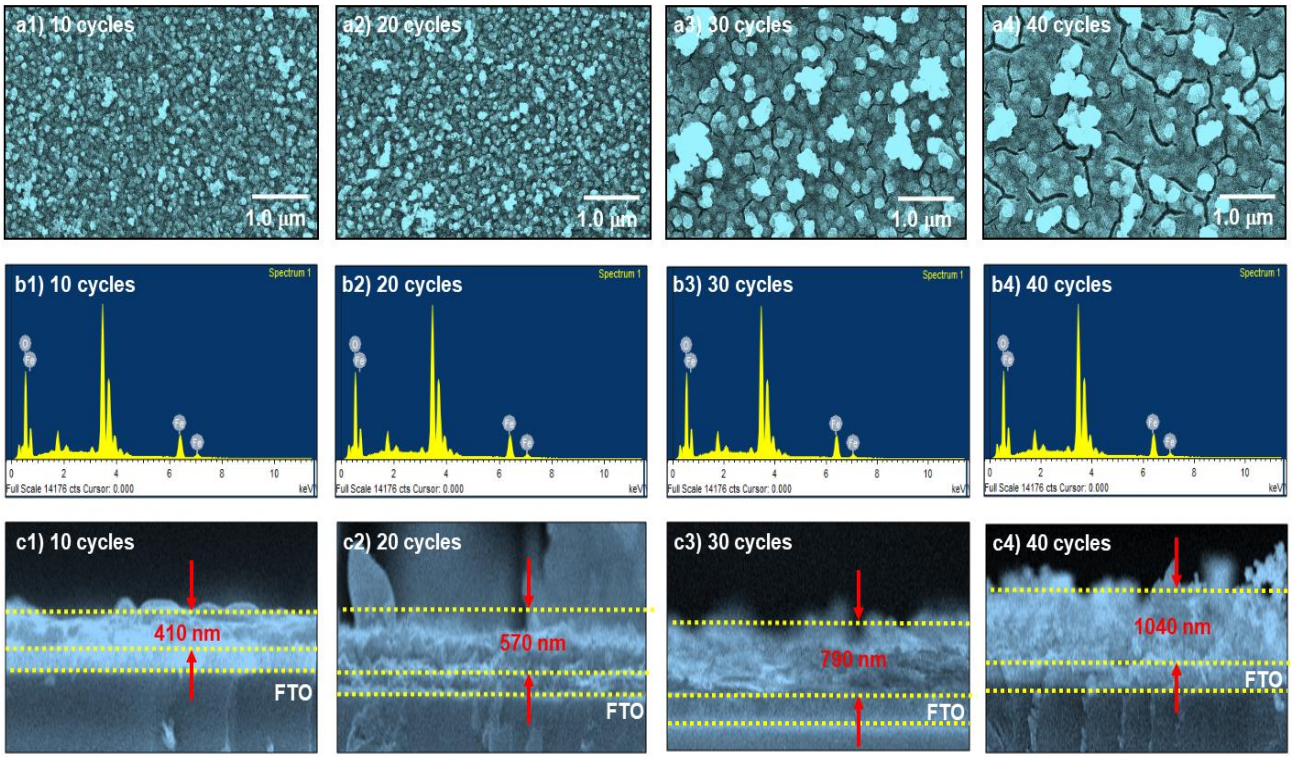

Fig. 4 Top view SEM images (a1-a4), EDS spectra (b1-b4), and cross-sectional SEM images (c1-c4) of α-Fe_2O_3 thin films deposited with potential cycles 10, 20, 30, and 40.

The EDS elemental mapping was carried out to analyze the elemental distribution of Fe and O in the Fe_2O_3 thin films. The elemental mapping data reveals the uniform distribution of both elements. Figs. 5(a1) - (a4) and Fig. 5(b1) - (b4) show the EDAX elemental mapping for Fe and O elements, respectively. The observation suggests the stoichiometry of all film samples, which is in good agreement with the expected ratio (Fe:O ≈ 2:3).

3.4 UV-Visible and PL spectroscopy analysis

The investigation of absorption properties of α-Fe_2O_3 is very crucial for its PEC application. Therefore, the optical properties of α-Fe_2O_3 films, such as absorbance and band gap, were investigated using UV-Visible spectroscopy. Fig. 6(a) shows the UV-Visible absorption spectra of α-Fe_2O_3 films deposited using the electrochemical deposition method at various potential cycles. The absorption edge in α-Fe_2O_3 films shifts towards a higher wavelength implying that α-Fe_2O_3 films absorb mainly in the visible region of the solar spectrum. The increment in the potential cycles of α-Fe_2O_3 films leads to an absorption improvement, advantageous for PEC application. Furthermore, the absorbance plot indicates the direct band gap of α-Fe_2O_3 films.

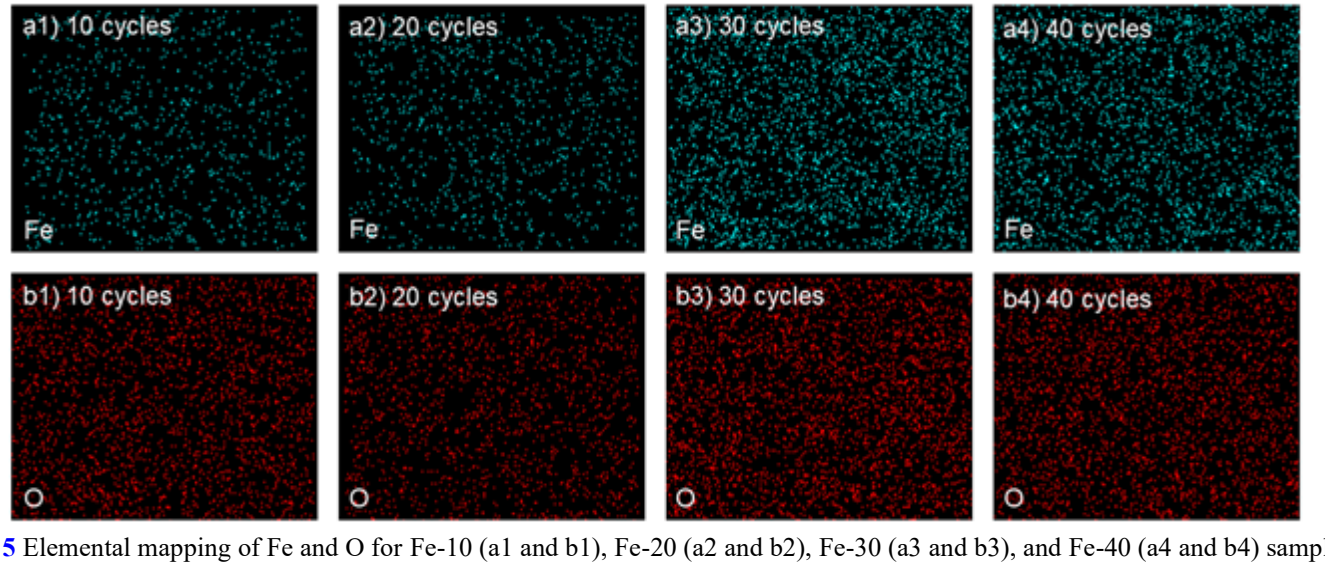

Fig. 5 Elemental mapping of Fe and O for Fe-10 (a1 and b1), Fe-20 (a2 and b2), Fe-30 (a3 and b3), and Fe-40 (a4 and b4) samples, respectively.

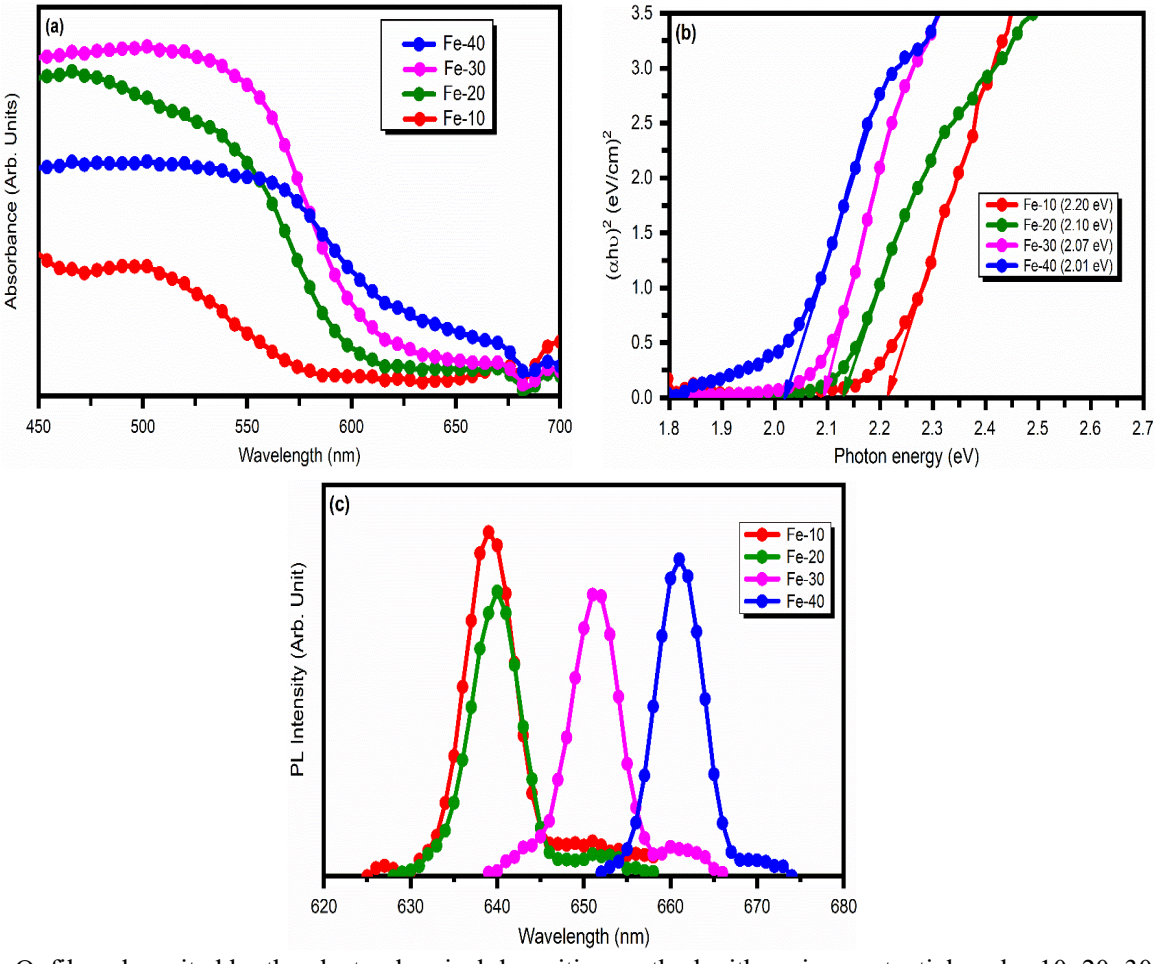

Fig. 6 α-Fe_2O_3 films deposited by the electrochemical deposition method with various potential cycles 10, 20, 30, and 40 (a) UV-Visible absorption spectra (b) Tauc plots, and (c) PL peak variation.

The energy-dependent absorption coefficient (α) can be expressed by the Equation (2):[44]

$$(\alpha h\nu)^{\frac{1}{\gamma}} = B\,(E - E_{opt}) \quad (2)$$

where h is the Planck constant, ν is the photon's frequency, E_{opt} is the bandgap energy, and B is the state optical density. The γ factor depends on the nature of the transition and is equal to 1/2 or 2 for the direct and indirect transition bandgaps, respectively.[45] The absorption coefficient (α) can be found from the films' transmittance using Equation (3):[46]

$$\alpha = \frac{1}{d} \ln\left[\frac{1}{T\,(\%)}\right] \quad (3)$$

where d and T are the thickness and transmittance of α-Fe_2O_3 films, respectively.

The optical band gap is estimated from the Tauc plot, which is obtained by plotting photon energy (hν) on the horizontal axis and $(\alpha h\nu)^2$ on the vertical axis. The linear extrapolation of $(\alpha h\nu)^2$ to the abscissa at zero permits the bandgap calculation. Fig. 6(b) shows the Tauc plots for α-Fe_2O_3 films deposited with various potential cycles. The band gap is decreased from 2.21 to 2.02 eV with increasing the potential cycle from 10 to 40. The reduction in the bandgap may be due to the increased α-Fe_2O_3 film thickness with an increase in potential cycles. It leads to good optical absorbance in the visible region and efficient separation of electron holes. However, the recombination of charge carriers increases with an increase in the thickness of thin films. The optical bandgap values calculated from the present study agree with the recently reported bandgap values of α-Fe_2O_3 films.[47,48]

The PL emission spectra of α-Fe_2O_3 films (Fig. 6(c)) were obtained from PL spectroscopy, and the tuning of PL peak with varying potential cycles 10, 20, 30, and 40 was observed. Moreover, the PL spectra of these films show substantial apparent Stokes shifts and full widths at half maximum (FWHM). Furthermore, it is also observed that the peaks of the PL were gradually red-shifted from 639 to 661 nm as the potential cycle was increased from 10 to 40, which is attributed to the increased film thickness and consequently increased absorption of film. The obtained results are consistent with a similar trend of red shift in optical bandgap values as seen in UV-Visible analysis. All the obtained PL peaks (639 to 661 nm) are attributed to ligand field electronic transition $6A_1 \rightarrow 4T_1$ (4G) of Fe^{3+} exhibited in the condensed phase.[49,50] The lower value of emission intensity of Fe-20 than that of Fe-10, Fe-30, and Fe-40 illustrates that the recombination rate of electron holes in the case of Fe-20 is lower than that of other samples.[51] This leads to a higher photocatalytic activity of Fe-20 than all other samples, as observed in Fig. 8 (discussed later).

3.5 X-ray photoelectron spectroscopy (XPS) analysis

The XPS measurements were carried out to gain an insight into the oxidation states and surface chemical composition of Fe_2O_3 thin films. Fig. 7(a) shows the typical XPS survey scan of α-Fe_2O_3 films deposited by the electrochemical deposition method for 20 potential cycles. The spectra were excited by Al k_α x-ray radiation (1486.6 eV) and calibrated against the C 1s line of carbon with the binding energy of 284.5 eV for hydrocarbon. The survey scan spectrum shows the iron (Fe 3p, Fe 3s, Fe 2p), carbon (C 1s), and oxygen (O 1s) peaks. The modes, in which most intense XPS lines occurred, were identified as elements 2p for Fe and 1s for O. These certain spectral lines were scanned with a high resolution (0.05 eV) to obtain details of the peak location and shapes in the region 700 to 740 eV for Fe 2p and 520 to 540 eV for O 1s. The peaks at 710.89 eV and 724.59 eV in the spectrum corresponding to the doublet of Fe $2p_{3/2}$ and Fe $2p_{1/2}$, respectively, can be attributed to the formation of Fe_2O_3.[52] For Fe $2p_{3/2}$ peaks, the major peak at 710.89 eV was attributed to Fe(III)-O, which corresponds to the Fe^{3+} chemical state. The C1s peak is usually present due to the adsorbed atmospheric hydrocarbons. Figs. 7(a) and fig. 7(b) shows the narrow scan for Fe 2p and O1s core-level x-ray photoelectron spectra of Fe_2O_3 film. The deconvoluted peaks for O1s are depicted in Fig. 7(b), which shows the main peak at 529.8 eV, and the shoulder peak at 531.45 eV attributed to the lattice (denoted as O^{2-}) and defect sites with low oxygen coordination, *i.e.*, oxygen vacancies on the sample surface. The core-level spectra of Fe display the x-ray photoelectron emission peaks for Fe $2p_{3/2}$ and Fe $2p_{1/2}$ at binding energies 710.89 and 724.59 eV, which are close to those of the standard values of Fe_2O_3. The characteristic spin-orbit splitting energy of 13.7 eV is clear evidence that Fe ions exist in the Fe^{3+} oxidation state of Fe_2O_3.[53] The elemental compositions of the films were calculated by Equation (4):

$$\%\,X = \frac{{}^{A_X}/_{S_X}}{\sum_{i=1}^{N} \frac{A_i}{S_i}} \quad (4)$$

where X is the element's name, A_X is the area under the peak of element X in the spectrum, and S_X is the sensitivity factor. For example, the sensitivity factors for iron $2p_{3/2}$ and oxygen are 1.971 and 0.711 eV, respectively.[54,55] From the compositional analysis, it is revealed that the surface of the formed Fe_2O_3 structure is oxygen deficient. The amount of oxygen is found to be ~ 73 % and that of Fe ~ 27 %. Thus, the composition calculated from XPS spectra for Fe:O is in good agreement. However, an excess amount of oxygen than Fe may be due to the adsorbed atmospheric oxygen at the surface of films.

3.6 Photoelectrochemical (PEC) measurements

The PEC measurements were carried out with the three-electrode system (Fig. 1), and the voltage variated from − 0.6 to 0.6 V *vs*. SCE in a 1.0 M NaOH electrolyte. Fig. 8 shows the PEC activity of α-Fe_2O_3 films photoanodes deposited using the electrochemical deposition method at various potential cycles. The PEC activity of the α-Fe_2O_3 films

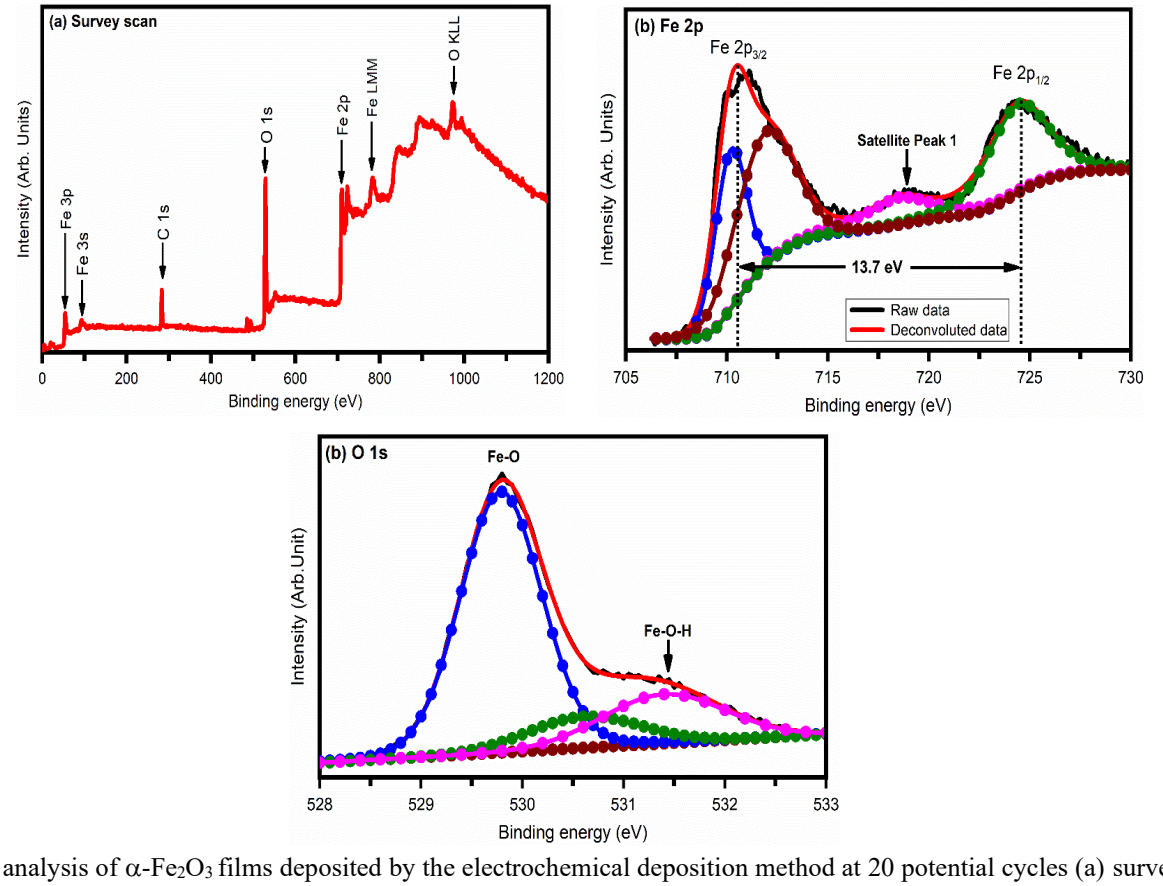

Fig. 7 XPS analysis of α-Fe_2O_3 films deposited by the electrochemical deposition method at 20 potential cycles (a) survey scan, (b) Fe 2P peak scan, and (c) O 1s with peaks related to Fe-O and Fe-OH bonds.

photoanode was evaluated using the linear sweep voltammetry (LSV). Fig. 8(a) shows the variation of photocurrent density (J) *vs* applied potential (V) for α-Fe_2O_3 films photoanodes deposited at various potential cycles. A minimal current of ~ 1 μA/cm^2 was observed for α-Fe_2O_3 film photoanode during the measurement of current density in the dark because of a non-faradic reaction.

However, under illumination, the photocurrent density increases with an increase in applied potential and potential cycles. In addition, no photocurrent saturation is observed for the positive bias, indicating better charge separation upon illumination. Also, compared to Fe-10, Fe-30, and Fe-40 photoanode, Fe-20 photoanodes showed a significantly enhanced photocurrent, which can be attributed to the higher light absorption and the rapid transport of carrier of α-Fe_2O_3 in the vicinity of electrolyte. It helps to harvest a large number of photons, leading to an increase in the number of charge carriers and thus an increase in photocurrent density. The high photocurrent density ~ 216 μA/cm^2 is observed at a bias voltage of 0.5 V *vs.* SCE under 100 mW/cm^2 illumination for the Fe-20 sample, which is a good PEC performance.

Furthermore, the time-dependent light pulsed photocurrent response or chronoamperometric photocurrent density-time profile (switching behavior) of the fabricated photoanodes was investigated at a bias potential of 0.5 V_{SCE} as shown in Fig. 8(b). Chronoamperometry measurements were used to test the photoresponse and stability of photoanodes. From the chronoamperometric photocurrent response, it is observed that with an increase in potential cycles from 10 to 40, the corresponding photoresponses were improved. More specifically, a rise of photocurrent of ~ 190 μA/cm^2, 216 μA/cm^2, 122 μA/cm^2, and 92 μA/cm^2 at 0.5 vs SCE under light illumination as compared to the dark condition of photoresponse ~ 0 μA/cm^2 were noticed for the photoanode film F-10, F-20, F-30 and F-40, respectively. The applied bias photon to current efficiency (ABPE) was calculated for α-Fe_2O_3 using Equation (5):

$$\text{ABPE} = \frac{J_{Ph}\,(1.23-|V_{Bias}|)}{P_{Light}} \quad (5)$$

where J_{Ph} is the photocurrent density (expressed in mA/cm^2), V_{Bias} is the applied external potential, and P_{Light} is the light source illumination intensity.[56] A maximum photon conversion efficiency of 1.44 % is obtained at a bias voltage of 1 V *vs*. SCE at a photocurrent density of 6.25 mA/cm^2 for the Fe-20 sample. The results are further supported by EIS analysis.

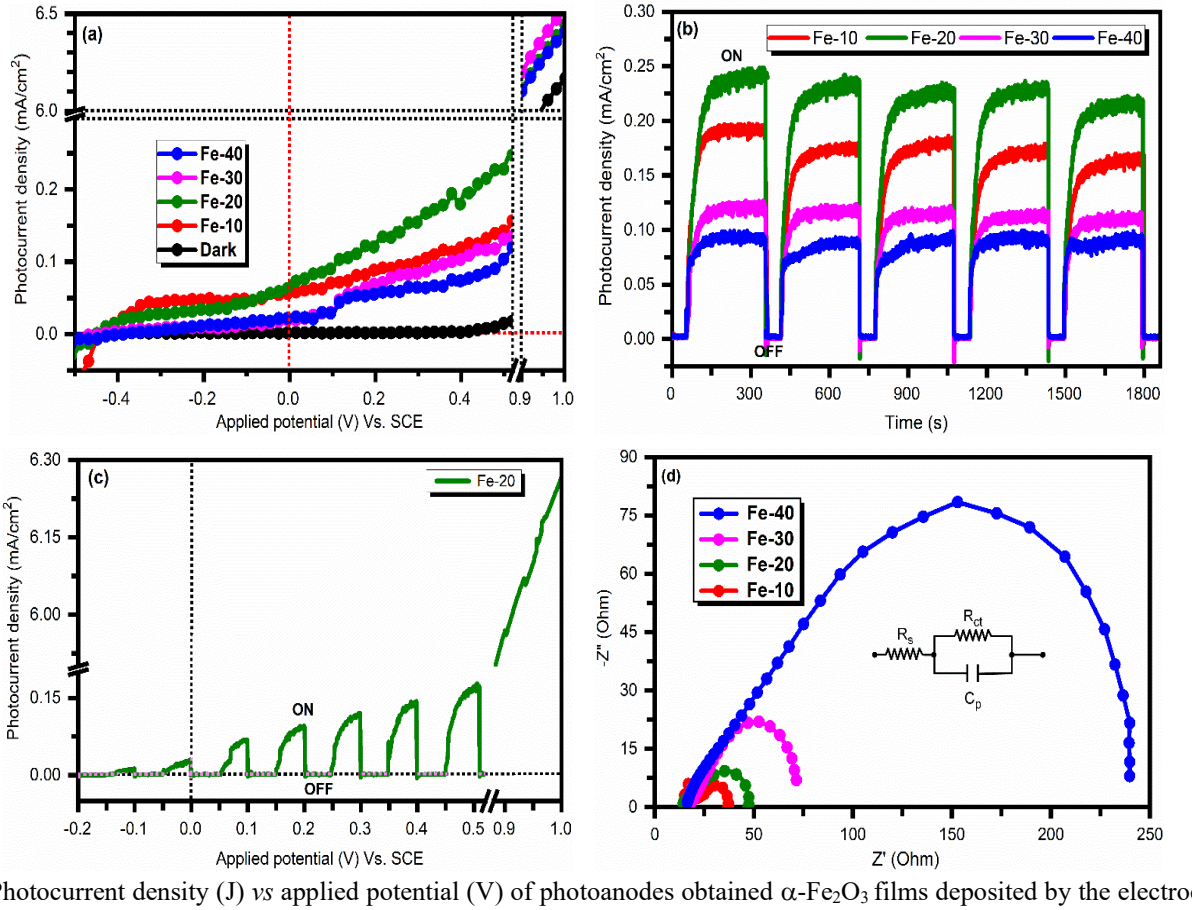

Fig. 8 (a) Photocurrent density (J) *vs* applied potential (V) of photoanodes obtained α-Fe_2O_3 films deposited by the electrochemical deposition method with various potential cycles, (b) chronoamperometric photocurrent density (J) – time (t) profile (switching behavior) of photoanodes obtained from α-Fe_2O_3 films deposited by the electrochemical deposition method with various potential cycles with chopped light at 0.5 V *vs*. SCE. (c) chopped LSV of α-Fe_2O_3 films deposited by the electrochemical deposition method at 20 potential cycles, and (d) Nyquist plots of the α-Fe_2O_3 electrode deposited using the electrochemical deposition method at various potential cycles.

To understand the improved PEC performance mechanism, the electrochemical kinetics, the charge transport, and transfer dynamics of the α-Fe_2O_3 photoanodes operated in 1 M NaOH electrolyte were also studied with EIS in a frequency range of 0.1 Hz to 100 kHz at a bias of 0.5 V *vs*. SCE under sunlight irradiation. Fig. 8(d) shows the Nyquist plots of the α-Fe_2O_3 electrode obtained from the EIS measurements. The Fe-10 and Fe-20 samples show a smaller impedance than Fe-30 and Fe-40 samples. Even though the impedance of Fe-10 is smaller than Fe-20, it also exhibits a higher recombination loss across the Fe-10 sample and electrolyte. The fitted equivalent electrical circuit is shown in the inset of Fig. 8(d). The fitted model consists of series resistance (R_s), interfacial charge transfer resistance (R_{ct}), the bulk capacitance of α-Fe_2O_3 (C_{bulk}), and the capacitance of the space charge layer at the interface Fe_2O_3/electrolyte (Csc).

Table 1. EIS analysis for α-Fe_2O_3 thin films prepared at different potential cycles.

Potential cycles	V_b (Volt)	R_s (Ohm)	R_{ct} (Ohm)
10	0.5	15	16
20	0.5	14	27
30	0.5	18	51
40	0.5	16	221

The Nyquist plot is a useful way to illustrate the semiconductor/electrolyte interfacial charge transfer process and the junction properties. The Nyquist plot arc radius represents the electron transfer resistance reflecting the electrode reaction energy barrier, and thus a decreased semicircle radii reflect a decrease in charge transfer resistance.[57] Resistance quantification analysis is shown in Fig. 8(d), indicating that all the photoanodes have a lower semicircle diameter (see Table 1). The lowest equivalent series resistance (R_s) obtained for all samples is ~ 14-18 Ω. As seen in Table 1, the charge transfer resistance (R_{ct}) value varies from a minimum value of 16 Ω for the Fe-10 sample to 221 Ω for the Fe-40 sample. All the synthesized samples show a considerable reduction in interfacial resistance between electrode and electrolyte, improving charge transfer efficiency. It may be due to the absorption of light and electron-hole pairs separation away from the interface. The incident photon creates an electron-hole pair upon absorption by photoanode as the electron moves from the valence band into the conduction band with a hole left behind in the valence band. The electron moves through the outer circuit to the counter electrode surface (Pt) and reduces the absorbed H^+ ions to produce H_2. The holes oxidize the OH^- ions that evolve oxygen at the semiconductor-electrolyte interface.[58] Due to much higher notches/cracks on the Fe-40 sample surface as observed in SEM, the photo-generated charge carriers cannot reach the FTO surface, eventually hinderi the carrier transport and thus reducing the photocurrent.

Our prepared photoanode is highly stable on the device level even after a long time (30 min) of light irradiation (photostable). The fabricated photoanode has passed the scotch tape test *i.e.*, good adhesive films. The comparison of our PEC performance result with the already reported values is shown in Table 2, along with various methods used to prepare hierarchical nanostructured α-Fe_2O_3 photoanodes. It is found that various methods have been used for the preparation of α-Fe_2O_3 photoanodes and the electrodeposition method was the most frequently used method, as indicated in Table 2. As per our knowledge, it has been observed that the electrodeposited α-Fe_2O_3 film showed the photoresponse with photocurrent density values in the range from the lowest 0.12 mA/cm^2 at 0.6 V_{SCE} to the highest 1.35 mA/cm^2 at 1.23 V_{SCE}.[43,59] In contrast, we have achieved the photocurrent density of 0.216 mA/cm^2 at 0.5 V_{SCE} or 6.25 mA/cm^2 at 1 V_{SCE} biased potential (Fig. 8(a)) with spherical morphology.

In comparing our observed photoresponse with the various preparation methods and morphologies, our results are much better while looking at the overall cost of the photoanode, which is evident from Table 2. Moreover, various composite photoanodes have been tried, namely, Au-α-Fe_2O_3, IOS-α-Fe_2O_3, and Au/Zr-Fe_2O_3/Au achieved photoresponses in a range of 1.30 to 8 mA/cm^2.[43,60,61] In comparison with the overall development in α-Fe_2O_3-based photoanodes, our results will encourage researchers to develop further 'Au' based composite photoanodes as reported by Mao *et al.*, where they reported the highest photocurrent density to date of 8 mA/cm^2 at 0.6 V using the same technique.[60]

3.7 Sample stability analysis

To ensure the stability of the samples after electrochemical measurement, we have further studied all samples via various characteristics using FTIR and XRD by Figs. 9(a-b). To ensure the structural and morphological stability of the samples after electrochemical measurement, the PEC-measured photoanode films were further investigated by FTIR and XRD, as shown in Figs. 9(a) and (b), respectively. The bonding configurations of the deposited thin films after photoelectrochemical measurements were investigated by the Fourier transform infrared (FTIR) spectroscopy. The FTIR spectra of the synthesized Fe_2O_3 thin films in the range of 550- 4000 cm^{-1} are shown in Fig 9(a). The broad bands observed between 3600-3000 cm^{-1} centered at ~ 3400 cm^{-1} are linked to the stretching O-H vibration of intermolecular and intramolecular hydrogen bonds in hydroxyl (OH^-) groups of the physically adsorbed water molecules after electrochemical analysis. The peaks ~ 1648 and ~ 1381 cm^{-1} are due to the H-O-H's asymmetric and symmetric bending vibration. The peak at 2352 cm^{-1} is related to atmospheric CO_2. The appearance of two well-defined peaks at 573 and 676 cm^{-1} is attributed to the Fe-O lattice vibrations in the stretching mode of the hematite phase of Fe_2O_3.[62–65] Furthermore, no significant changes in intensity and peak position of all samples were noticed in the XRD pattern of all films after PEC measurements. Also, the surface morphology and compactness of all films observed

through SEM images were found to be unchanged [Figs. 10 (a)-(d)]. Hence, there is no significant effect of PEC measurement on the quality of prepared film using electrodeposition.

Table 2. Comparison of PEC performance of hierarchical nanostructured α-Fe_2O_3 photoanodes prepared by various methods.

Material	Morphology	Synthesis method	Electrolyte	PEC performance	Ref.
α-Fe_2O_3	Worm-like	Sol-Gel method	0.1 M Na_2SO_4	11 μA/cm^2 at 0.57 $V_{Ag/AgCl}$	[32]
α-Fe_2O_3	Particles structure	Pulsed plasma	0.1 M Na_2SO_4	186.7 μA/cm^2 at 0.57 $V_{Ag/AgCl}$	[32]
α- Fe_2O_3	Nanoparticles	Electrodeposition	1M KOH	1.35 mA/cm^2 at 1.23 V	[43]
Au/Zr- Fe_2O_3/Au	Spherical particle	Electrodeposition	1 M NaOH	1.30 mA/cm^2	[43]
α-Fe_2O_3	Granule in nature	Electrodeposition	1 M NaOH	0.12 mA/cm^2 At 0.6 V/SCE	[59]
Au-α- Fe_2O_3	nanorods	Electrodeposition	1 M NaOH	8 mA/cm^2 At 0.6V vs Ag/AgCl	[60]
IOS-α- Fe_2O_3	Nanoparticles	Electrodeposition	1 M NaOH	3.1 mA/cm^2 0.5 V Ag/AgCl	[61]
α-Fe_2O_3	Islands of Particles	Electrodeposition	1 M NaOH	390 μA/cm^2 at 0.4 $V_{Ag/AgCl}$	[66]
α- Fe_2O_3	nano pedals	Pulse reverse electrodeposition	1 M NaOH	0.75 mA/cm^2 0.65 V Ag/AgCl	[67]
α-Fe_2O_3	Nanoflakes	AACVD	0.5 M Na_2SO_4 0.1 M Na_2SO_3	585 uA/cm^2 Ag/AgCl at 1.23 V	[68]
α-Fe_2O_3	Nanoparticle	Electrodeposition	1 M NaOH	257.08 uA Ag/AgCl at 1.23 V	[69]
α-Fe_2O_3	Nanorods	Hydrothermal	1 M KOH	0.45 mA/cm^2 Ag/AgCl at 1.23V	[70]
α-Fe_2O_3	Agglomerated	Pulse reverse electrodeposition	1 M NaOH	504 uA/cm^2 1.23 V_{RHE}	[71]
α-Fe_2O_3	Mesoporous nature	Hydrothermal-electrodeposition	1M NaOH	43.7uA/cm^2	[72]
α- Fe_2O_3	Nanoparticles	Thermal decomposition	1M NaOH	3 mA/cm^2 At 1.23 V_{RHE}	[73]
α-Fe_2O_3	Spherical particles	Electrodeposition	1 M NaOH	216 μA/cm^2 at 0.5 V_{SCE} and 6.25 mA/cm^2 at 1 V_{SCE}	Present Work

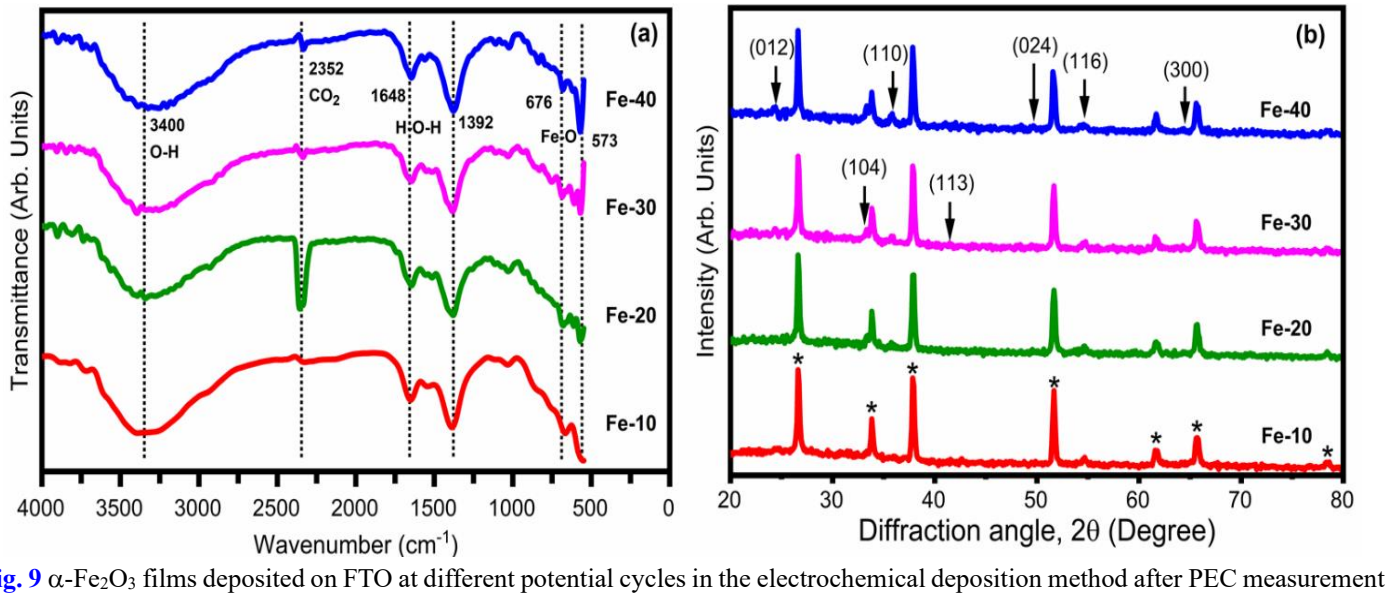

Fig. 9 α-Fe_2O_3 films deposited on FTO at different potential cycles in the electrochemical deposition method after PEC measurement (a) FTIR spectra (b) XRD pattern.

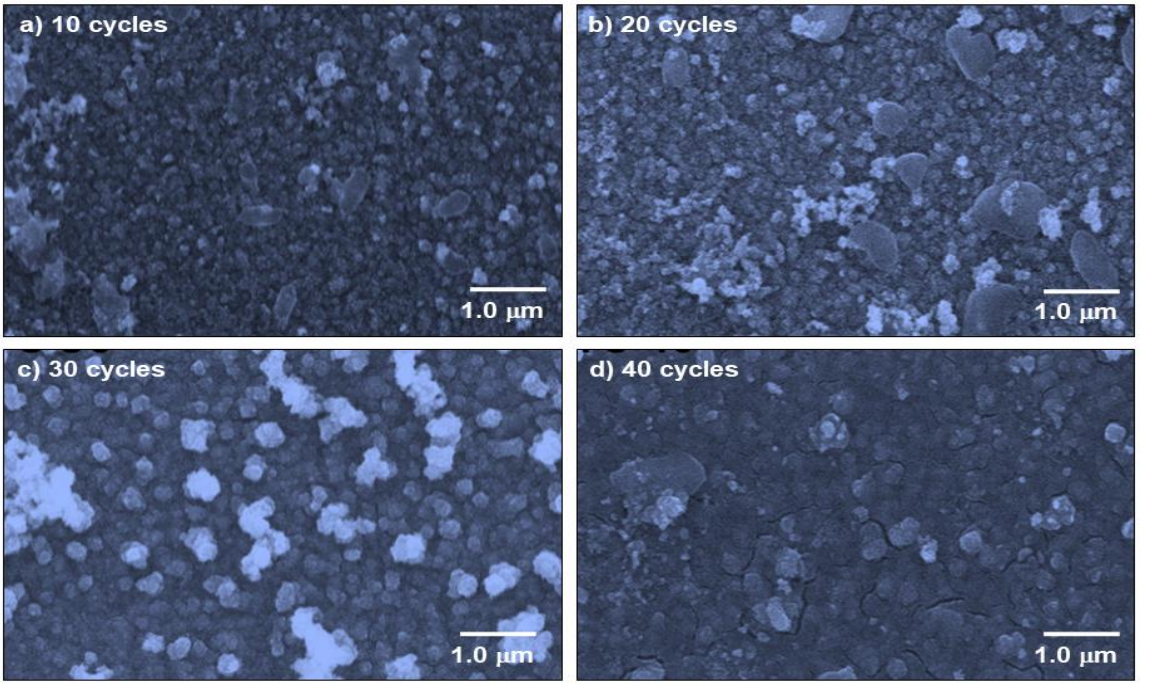

Fig. 10 (a-d) SEM images of α-Fe_2O_3 electrodes after PEC measurements.

The present photocatalytic system offers a facile and straightforward water-splitting cell development technique, although it suffers from the poor separation of charge carriers and surfaces back reaction. Furthermore, the combination of α-Fe_2O_3 with wide band gaps in nano-structured semiconductors like ZnO and TiO_2 can further improve the water-splitting performance.

4. Conclusions

The hematite-Fe_2O_3 (α-Fe_2O_3) thin-film photoelectrodes were synthesized using a facile and cost-effective electrodeposition technique with various potential cycles corresponding to different thicknesses of deposited films. The as-prepared α-Fe_2O_3 thin films have been characterized by XRD and Raman spectroscopy, which confirm the formation of α-Fe_2O_3. SEM analysis showed that the α-Fe_2O_3 thin films deposited with 10 and 20 potential cycles revealed dense and uniform growth with granular morphology of Fe_2O_3 on the FTO surface with very few defects. However, the deposited films with more deposition cycles showed notches on the film surface. The elemental composition analysis of α-Fe_2O_3 films performed using the EDS, and XPS analysis showed that the Fe and O elemental compositions are close to the stoichiometric ratio 2:3 in all films and with the Fe^{3+} and O^{2-} chemical states. UV-visible spectroscopy shows that α-Fe_2O_3 absorbs mainly in the visible region, and the bandgap decreases from 2.21 to 2.02 eV with an increase in potential cycles from 10 to 40. PEC and EIS measurements were used to evaluate the suitability of α-Fe_2O_3 thin films for photoanode. A maximum photon conversion efficiency of 1.44% was obtained with a photocurrent density of 6.25 mA/cm^2 at 1 V *vs*. SCE under simulated solar light. The prepared photoanode was highly stable against all pH conditions, and no photobleaching was observed for up to 30 min with the stability analysis. We believe that combining α-Fe_2O_3 with wide band gap nano-structured semiconductors like ZnO, and Ti O_2 can further improve the solar water splitting performance.

Acknowledgments

AVR and YAJ thank SPPU PDF (Grant No. SPPU-PDF/ST/PH/2021/0005 and PDF/ST/CH/2019/0004) and Department of Physics and School of Energy Studies, SPPU, for financial support and laboratory facilities access. SRR and NYD acknowledge the UK Engineering and Physical Sciences Research Council (EPSRC) for funding (Grant No. EP/S001395/1). Sandesh Jadkar is thankful to the Indo-French Centre for the Promotion of Advanced Research-CEFIPRA, Department of Science and Technology, New Delhi, for financial support.

Conflict of interest

There are no conflicts to declare.

Supporting information

Not applicable.

References

[1] J. Nowotny, C. Sorrell, L. Sheppard, T. Bak, *International Journal of Hydrogen Energy*, 2005, **30**, 521-544, doi: 10.1016/j.ijhydene.2004.06.012.

[2] R. Krol, Y. Liang, J. Schoonman, *Journal of Materials Chemistry*, 2008, **18**, 2311-2320, doi: 10.1039/b718969a.

[3] S. Rajaambal, K. Sivaranjani, C. S. Gopinath, *Journal of Chemical Sciences*, 2015, **127**, 33-47, doi: 10.1007/s12039-014-0747-0.

[4] A. Fujishima, K. Honda, *Nature*, 1972, **238**, 37-38, doi:

10.1038/238037a0.
[5] H. Cheng, W. Chiu, C. Lee, S. Tsai, W. Hsieh, *The Journal of Physical Chemistry C*, 2008, **112**, 16359-16364, doi: 10.1021/jp805239k.
[6] A. Rokade, S. Rondiya, V. Sharma, M. Prasad, H. Pathan, S. Jadkar, *Journal of Solid State Electrochemistry*, 2017, **21**, 2639-2648, doi: 10.1007/s10008-016-3427-9.
[7] W. Chen, G. B. Huang, H. Song, J. Zhang, *Journal of Materials Chemistry A*, 2020, **8**, 20963-20969, doi: 10.1039/d0ta06177h.
[8] Y. Zhang, L. Han, C. Wang, W. Wang, T. Ling, J. Yang, C. Dong, F. Lin, X. W. Du, *ACS Catalysis*, 2017, **7**, 1470-1477, doi: 10.1021/acscatal.6b03212.
[9] H. J. Lee, J. Bang, J. Park, S. Kim, S. M. Park, *Chemistry of Materials*, 2010, **22**, 5636-5643, doi: 10.1021/cm102024s.
[10] P. Brázda, J. Kohout, P. Bezdička, T. Kmječ, *Crystal Growth & Design*, 2014, **14**, 1039-1046, doi: 10.1021/cg4015114.
[11] S. B. Jathar, S. R. Rondiya, Y. A. Jadhav, D. S. Nilegave, R. W. Cross, S. V. Barma, M. P. Nasane, S. A. Gaware, B. R. Bade, S. R. Jadkar, A. M. Funde, N. Y. Dzade, *Chemistry of Materials*, 2021, **33**, 1983-1993, doi: 10.1021/acs.chemmater.0c03223.
[12] A. Rokade, S. Rondiya, A. Jadhavar, S. Pandharkar, S. Karpe, K. Diwate, S. Jadkar, *2nd International Conference on Emerging Technologies: Micro to Nano 2015*, 2016, **1724**, 20009.
[13] K. Sivula, F. Le Formal, M. Grätzel, *ChemSusChem*, 2011, **4**, 432-449, doi: 10.1002/cssc.201000416.
[14] F. Leandro Souza, K. P. Lopes, E. Longo, E. R. Leite, *Physical Chemistry Chemical Physics*, 2009, **11**, 1215, doi: 10.1039/b811946e.
[15] M. Mishra, D. M. Chun, *Applied Catalysis A: General*, 2015, **498**, 126-141, doi: 10.1016/j.apcata.2015.03.023.
[16] D. K. Zhong, M. Cornuz, K. Sivula, M. Grätzel, D. R. Gamelin, *Energy & Environmental Science*, 2011, **4**, 1759, doi: 10.1039/c1ee01034d.
[17] K. Cao, L. Jiao, H. Liu, Y. Liu, Y. Wang, Z. Guo, H. Yuan, *Advanced Energy Materials*, 2015, **5**, 1401421, doi: 10.1002/aenm.201401421.
[18] X. Zhu, Y. Zhu, S. Murali, M. D. Stoller, R. S. Ruoff, *ACS Nano*, 2011, **5**, 3333-3338, doi: 10.1021/nn200493r.
[19] C. Zhao, X. Shao, Y. Zhang, X. Qian, *ACS Applied Materials & Interfaces*, 2016, **8**, 30133-30142, doi: 10.1021/acsami.6b09594.
[20] H. Saada, R. Abdallah, J.-F. Bergamini, S. Fryars, V. Dorcet, L. Joanny, F. Gouttefangeas, S. Ollivier, G. Loget, *ChemElectroChem*, 2020, **7**, 1155-1159, doi: 10.1002/celc.202000028.
[21] J. Krysa, M. Zlamal, S. Kment, Z. Hubicka, *Chemical Engineering Transactions*, 2014, **41**, 379-384, doi: 10.3303/CET1441064.
[22] N. Gupta, Y. Ghaffari, J. Bae, K. Kim, *Journal of Molecular Liquids*, 2020, **301**, 112473, doi: 10.1016/j.molliq.2020.112473.
[23] L. Li, G. Zhou, Z. Weng, X. Y. Shan, F. Li, H. M. Cheng, *Carbon*, 2014, **67**, 500-507, doi: 10.1016/j.carbon.2013.10.022.
[24] R. Li, Y. Jia, N. Bu, J. Wu, Q. Zhen, *Journal of Alloys and Compounds*, 2015, **643**, 88-93, doi: 10.1016/j.jallcom.2015.03.266.
[25] N. A. Arzaee, M. F. Mohamad Noh, A. Ab Halim, M. A. F. Abdul Rahim, N. A. Mohamed, J. Safaei, A. Aadenan, S. N. Syed Nasir, A. F. Ismail, M. A. Mat Teridi, *Ceramics International*, 2019, **45**, 16797-16802, doi: 10.1016/j.ceramint.2019.05.219.
[26] W. Hamd, S. Cobo, J. Fize, G. Baldinozzi, W. Schwartz, M. Reymermier, A. Pereira, M. Fontecave, V. Artero, C. Laberty-Robert, C. Sanchez, *Physical Chemistry Chemical Physics*, 2012, **14**, 13224, doi: 10.1039/c2cp42535a.
[27] P. Maneeratanasarn, T. Van Khai, S. Y. Kim, B. G. Choi, K. B. Shim, *Physica Status Solidi (a)*, 2013, **210**, 563-569, doi: 10.1002/pssa.201228427.
[28] J. Lin, X. Zhang, L. Zhou, S. Li, G. Qin, *Materials Research Bulletin*, 2017, **91**, 214-219, doi: 10.1016/j.materresbull.2017.03.060.
[29] M. Tadic, M. Panjan, V. Damnjanovic, I. Milosevic, *Applied Surface Science*, 2014, **320**, 183-187, doi: 10.1016/j.apsusc.2014.08.193.
[30] K. Abass, *International Letters of Chemistry, Physics and Astronomy*, 2015, **45**, 24-31, doi: 10.18052/www.scipress.com/ilcpa.45.24.
[31] M. Mahadik, S. Shinde, V. Mohite, S. Kumbhar, K. Rajpure, A. Moholkar, J. Kim, C. Bhosale, *Materials Express*, 2013, **3**, 247-255, doi: 10.1166/mex.2013.1120.
[32] J. Krysa, M. Zlamal, S. Kment, M. Brunclikova, Z. Hubicka, *Molecules*, 2015, **20**, 1046-1058, doi: 10.3390/molecules20011046.
[33] B. Klahr, T. Hamann, The Journal of Physical Chemistry C, 2011, **115**, 8393-8399, doi: 10.1021/jp200197d.
[34] H. Dotan, K. Sivula, M. Grätzel, A. Rothschild, S. C. Warren, *Energy Environ Sci*, 2011, **4**, 958-964, doi: 10.1039/c0ee00570c.
[35] P. Sharma, J. W. Jang, J. S. Lee, *ChemCatChem*, 2019, **11**, 157-179, doi: 10.1002/cctc.201801187.
[36] J. Kennedy, K. Frese, *Journal of the Electrochemical Society*, 1978, **125**, 709-714, doi: 10.1149/1.2131532.
[37] A. Murphy, P. Barnes, L. Randeniya, I. Plumb, I. Grey, M. Horne, J. Glasscock, *International Journal of Hydrogen Energy*, 2006, **31**, 1999-2017, doi: 10.1016/j.ijhydene.2006.01.014.
[38] W. Qu, S. Weng, L. Zhang, M. Sun, B. Liu, W. Du, Y. Zhang, *Applied Physics Express*, 2020, **13**, 121001, doi: 10.35848/1882-0786/abc5fa.
[39] X. Hu, Jimmy C. Yu, J. Gong, *The Journal of Physical Chemistry C*, 2007, **111**, 11180-11185.
[40] B. Cullity, Elements of X-ray Diffraction, *Addison-Wesley Publishing*, 1956.
[41] D. Faria, S. Silva, M. Oliveira, *Journal of Raman Spectroscopy*, 1997, **28**, 873-878, doi: 10.1002/(sici)1097-4555(199711)28:11<873::aid-jrs177>3.0.co;2-b.
[42] K. Fleischer, O. Mauit, I. V. Shvets, *Applied Physics Letters*, 2014, **104**, 192401, doi: 10.1063/1.4876059.
[43] Q. Zeng, J. Bai, J. Li, L. Xia, K. Huang, X. Li, B. Zhou, *Journal of Materials Chemistry A*, 2015, **3**, 4345-4353, doi: 10.1039/c4ta06017b.
[43] Q. Zeng, J. Bai, J. Li, L. Xia, K. Huang, X. Li, B. Zhou, *Journal of Materials Chemistry A*, 2015, **3**, 4345-4353, doi:

10.1039/c4ta06017b.
[45] J. I. Pankove, D. A. Kiewit, *Journal of the Electrochemical Society*, 1972, **119**, 156C, doi: 10.1149/1.2404256.
[46] J. Tauc, *Materials Research Bulletin*, 1970, **5**, 721-729, doi: 10.1016/0025-5408(70)90112-1.
[47] A. Demircioğlu, K. Ç. Demir, *Journal of Electronic Materials*, 2021, **50**, 2750-2760, doi: 10.1007/s11664-021-08786-y.
[48] S. Singh, N. Goswami, *Current Applied Physics*, 2021, **22**, 20-29, doi: 10.1016/j.cap.2020.11.009.
[49] S. Singh, G. Hitkari, G. Pandey, *Inorganic and Nano-Metal Chemistry*, 2018, **48**, 477-485, doi: 10.1080/24701556.2019.1571511.
[50] S. Mitra, S. Das, K. Mandal, S. Chaudhuri, *Nanotechnology*, 2007, **18**, 275608, doi: 10.1088/0957-4484/18/27/275608.
[51] D. Muthee, B. Dejene, *Heliyon*, 2021, **7**, e07269, doi: 10.1016/j.heliyon.2021.e07269.
[52] H. Wang, J. Mao, Z. Zhang, Q. Zhang, L. Zhang, P. Li, *Toxins*, 2019, **11**, 105, doi: 10.3390/toxins11020105.
[53] V. L. Tauson, D. N. Babkin, T. M. Pastushkova, V. V. Akimov, T. S. Krasnoshchekova, S. V. Lipko, O. Y. Belozerova, *Geochemistry International*, 2012, **50**, 227-245, doi: 10.1134/s001670291203010x.
[54] M. C. Biesinger, B. P. Payne, A. P. Grosvenor, L. W. M. Lau, A. R. Gerson, R. St. C. Smart, *Applied Surface Science*, 2011, **257**, 2717-2730, doi: 10.1016/j.apsusc.2010.10.051.
[55] M. E. A. Warwick, K. Kaunisto, G. Carraro, A. Gasparotto, C. Maccato, D. Barreca, *Surface Science Spectra*, 2015, **22**, 47-57, doi: 10.1116/11.20150202.
[56] Z. Chen, T. F. Jaramillo, T. G. Deutsch, A. Kleiman-Shwarsctein, A. J. Forman, N. Gaillard, R. Garland, K. Takanabe, C. Heske, M. Sunkara, E. W. McFarland, K. Domen, E. L. Miller, J. A. Turner, H. N. Dinh, *Journal of Materials Research*, 2010, **25**, 3-16, doi: 10.1557/jmr.2010.0020.
[57] A. Verma, A. Srivastav, D. Sharma, A. Banerjee, S. Sharma, V. R. Satsangi, R. Shrivastav, D. K. Avasthi, S. Dass, *Nuclear Instruments and Methods in Physics Research Section B: Beam Interactions With Materials and Atoms*, 2016, **379**, 255-261, doi: 10.1016/j.nimb.2016.04.006.
[58] Z. Chen, W. Wei, B. J. Ni, *Current Opinion in Green and Sustainable Chemistry*, 2021, **27**, 100398, doi: 10.1016/j.cogsc.2020.100398.
[59] P. Kumar, P. Sharma, R. Shrivastav, S. Dass, V. R. Satsangi, *International Journal of Hydrogen Energy*, 2011, **36**, 2777-2784, doi: 10.1016/j.ijhydene.2010.11.107.
[60] A. Mao, G. Han, J. Park, *Journal of Materials Chemistry*, 2010, **20**, 2247–2250, doi: 10.1039/b921965j.
[61] X. Shi, K. Zhang, K. Shin, J. H. Moon, T. W. Lee, J. H. Park, *Physical Chemistry Chemical Physics*, 2013, **15**, 11717, doi: 10.1039/c3cp50459j.
[62] M. Bulinski, I. Iova, A. Belea, V. Kuncser, G. Filoti, *Journal of Materials Science Letters*, 2000, **19**, 27-28, doi: 10.1023/a:1006739412409.
[63] Z. Luo, C. Li, S. Liu, T. Wang, J. Gong, *Chemical Science*, 2017, **8**, 91-100, doi: 10.1039/c6sc03707k.
[64] S. Sobhanardakani, A. Jafari, R. Zandipak, A. Meidanchi, *Process Safety and Environmental Protection*, 2018, **120**, 348-357, doi: 10.1016/j.psep.2018.10.002.
[65] C. Y. Cao, J. Qu, W. S. Yan, J. F. Zhu, Z. Y. Wu, W. G. Song, *Langmuir*, 2012, **28**, 4573-4579, doi: 10.1021/la300097y.
[66] G. Rahman, O. Joo, *Materials Chemistry and Physics*, 2013, **140**, 316-322, doi: 10.1016/j.matchemphys.2013.03.042.
[67] P. Shinde, G. Go, W. Lee, *Journal of Materials Chemistry*, 2012, **22**, 10469-10471, doi: 10.1039/c2jm31254a.
[68] G. Wang, Y. Ling, D. A. Wheeler, K. E. N. George, K. Horsley, C. Heske, J. Z. Zhang, Y. Li, *Nano Letters*, 2011, **11**, 3503-3509, doi: 10.1021/nl202316j.
[69] P. Liang, L. Li, C. Liu, W. Wang, H. Zhang, N. Mitsuzaki, Z. Chen, *Thin Solid Films*, 2018, **666**, 161-171, doi: 10.1016/j.tsf.2018.09.034.
[70] T. T. Li, Q. Zhou, J. Qian, Y. Hu, Y. Q. Zheng, *Electrochimica Acta*, 2019, **307**, 92-99, doi: 10.1016/j.electacta.2019.03.183.
[71] P. S. Shinde, A. Annamalai, J. Y. Kim, S. H. Choi, J. S. Lee, J. S. Jang, *The Journal of Physical Chemistry C*, 2015, **119**, 5281-5292, doi: 10.1021/jp5100186.
[72] C. Yilmaz, U. Unal, *RSC Advances*, 2016, **6**, 8517-8527, doi: 10.1039/c5ra20105e.
[73] S. Tilley, M. Cornuz, K. Sivula, M. Grätzel, *Angewandte Chemie International Edition*, 2010, **49**, 6405-6408, doi: 10.1002/anie.201003110.

Author Information

Avinash V. Rokade *completed two Master's Degrees (M.Sc. in 2012 and M.Phil. in 2014). He has gained expertise in nanomaterial synthesis by the chemical route and their application for photocatalytic water splitting for hydrogen gas evolution. He was awarded NREF (National Renewable Energy Fellowship) of MNRE, Govt. of India to pursue a Ph. D. at the School of Energy Studies, Savitribai Phule Pune University, from 2014 to 2018. He has been awarded a Ph. D. in physics from the Department of Physics, Savitribai Phule Pune University, Pune, in 2018. He has published more than 35 research articles and 2 book chapters in peer-reviewed journals. Presently, he is working as Savitribai Phule Postdoctoral Fellow (SPPU PDF) at the Department of Physics, Savitribai Phule Pune University, Pune, working in the field of optoelectronic devices, solar energy harvesting, and battery, supercapacitor energy storage, mainly to improve cell efficiency with the help of 1D, 2D, and 3D nanostructures and investigation of their interfacial properties via photoelectrochemical impedance spectroscopy, cyclic voltammetry, Chrono methods, and Mott-Schottky analysis for photo-generated charge-transfer dynamics, band alignment, and band engineering.*

Yogesh A. Jadhav *is currently working as Savitribai Phule Postdoctoral Fellow (SPPU PDF) at the School of Energy Studies, Savitribai Phule Pune University. He has obtained his MS degree in Nanotechnology with 1st Rank. He was awarded DST INSPIRE Fellowship (2013) for Pursuing his Ph.D. in Physical Chemistry (2018) from Savitribai Phule Pune University, Pune. He has worked as Scientist C in National Centre for Nanoscience and Nanotechnology Mumbai University, Mumbai (2019). His research is focused on Semiconductor Nanocrystals/Quantum dot Synthesis, thin-film deposition, Electrochemistry for energy harvesting and storage devices like Solar cells, Batteries, and Supercapacitors.*

Ganesh K. Rahane *is a Research Scholar at the Department of Physics and School of Energy Studies, Savitribai Phule Pune University, Pune 411 007 (India).*

Sagar Jathar *is currently working as a Research Scholar at the School of Energy Studies, Savitribai Phule Pune University, Pune 411007 (India). His research interest area includes synthesis of chalcogenide novel semiconductor nanomaterials and investigation of Structural, Optical, and Photoelectrochemical and their heterostructures for Photovoltaic applications.*

Swati Rahane *has completed her Masters in Physics (Nanotechnology) from the Department of Physics, Savitribai Phule Pune University (Formerly University of Pune), Pune-411 007, India. She has worked as a Technical Assistant on a research project entitled "Studies of Al-doped Zinc Oxide Nanocrystals" in 2017. Currently, she is working as a Ph.D. Scholar in Department of Physics, University of Pune. Her research interest is in Semiconductor Nanocrystals/Quantum dots synthesis, thin-film fabrication, and Energy Harvesting. Her Ph.D. work mainly focuses on studying giant electron-phonon coupling in Halide Double Perovskites, understanding the photovoltaic performance limiting factors, and insights into the carrier dynamics to study defects present in the material.*

Shruti Shah *is currently working Junior Research Fellow (MNRE) at the School of Energy Studies, Savitribai Phule Pune University, Pune 411 007. Her research interest area includes the study and synthesis of Lead-free metal Halide Perovskite for photovoltaic applications.*

Nelson Dzade *is an EPSRC Innovation Research Fellow and leads the Materials Research Driven by Computation Group in the School of Chemistry at Cardiff University. Nelson received his Ph.D. from the University College London (UCL) in 2014, where he worked on "Unraveling the interactions of organic molecules with the surfaces of iron-bearing minerals." He then worked as a postdoctoral researcher at Utrecht University, The Netherlands, on the "Computer-aided design of iron-sulfide nanocatalysts for the solar-driven conversion of CO_2 to fuels". He was awarded the prestigious EPSRC Innovation Fellowship in 2018, and he has since become an Independent Research Group Leader in the School of Chemistry, Cardiff University. He was also awarded the DUO-India Professor Fellowship Award in 2020, enabling him to establish high-profile collaborations with leading Indian Scientists.*

Sandesh R. Jadkar *is Senior Professor in Physics at Department of Physics and Director, School of Energy Studies, Savitribai Phule Pune University, Pune 411 007 (India). He completed M. Sc. and Ph. D. degrees in Physics from Savitribai Phule Pune University in 1990 and 2001, respectively, followed by postdoctoral training at Laboratory of Physics of Interfaces and Thin Films (LPICM), Ecole Polytechnique, Palaiseau, France (2002-2003), and Department of Physics, Camerino University, Italy (2008-2009). He is a Fellow of the Maharashtra Academy of Sciences. His research focuses mainly on low-cost thin-film solar cells, water splitting, photodetectors and sensors, and 2D materials. So far, 22 students have completed their Ph. D. and 11 students are working for Ph. D. under his supervision. He has published more than 250 research articles in peer-reviewed international journals and published 03 book chapters.*

Publisher's Note: Engineered Science Publisher remains neutral with regard to jurisdictional claims in published maps and institutional affiliations.